Radiative decay rate and branching fractions of MgF

E. B. Norrgard [1,*], Yuly Chamorro [2], C. C. Cooksey [1], S. P. Eckel [1], N. H. Pilgram [1], K. J. Rodriguez [1,3],
H. W. Yoon [1], Lukáš F. Pašteka [2,4] and Anastasia Borschevsky [2]

[1]*Sensor Science Division, National Institute of Standards and Technology, Gaithersburg, Maryland 20899, USA*
[2]*Van Swinderen Institute for Particle Physics and Gravity, University of Groningen, Nijenborgh 4, 9747AG Groningen, The Netherlands*
[3]*University of Maryland, College Park, Maryland, USA*
[4]*Department of Physical and Theoretical Chemistry, Faculty of Natural Sciences,
Comenius University, Mlynská dolina, 84215, Bratislava, Slovakia*

We report measured and calculated values of radiative decay rates and vibrational branching fractions for the $A\,^2\Pi(v=0)$ state of $^{24}\mathrm{Mg}\,^{19}\mathrm{F}$. The decay rate measurements use time-correlated single-photon counting with roughly 1% total uncertainty. Branching-fraction measurements are performed using two calibrated imaging systems to achieve few percent total uncertainty. We use the multireference relativistic *ab initio* methods to calculate the Franck-Condon factors and transition dipole moments required to determine the decay rates and the branching fractions. The measurements provide a precision benchmark for testing the accuracy of the molecular structure calculations. The determination of the decay rate and vibrational branching fractions can be used to inform future optical cycling and laser cooling schemes for the MgF molecule.

I. INTRODUCTION

Recently, magneto-optical traps containing a record number $N \approx 10^5$ trapped molecules were demonstrated for CaF [1] and YO [2]. Further increasing the number of molecules trapped is desirable for several laser-cooled molecule applications. Studies of cold collisions and cold chemistry [3–5] require high reaction rates, motivating a large N to achieve a high molecule density. Because signal-to-noise ratios generally are proportional to $\sqrt{N}$, molecule-based sensors [6,7] directly benefit. Other applications, such as quantum information and quantum simulation [8–10], require low temperature T rather than large N. Because the ultimate step in cooling is often evaporation [11], which sacrifices N to achieve lower T, such applications also benefit from a large initial N.

Efficient slowing of molecular beams is vital to achieve a large trapped molecule number N. A large deceleration a from laser slowing [12] is desired because the distance required to stop molecules d is proportional to $1/\sqrt{a}$. Additionally, as molecules are slowed, the molecular beam brightness falls as $1/d^2$ if the beam's transverse velocity distribution is not modified. Thus, simple scaling arguments show that the trapped molecule number N, which is proportional to beam brightness, is proportional to a. Simultaneously applying transverse radiative cooling and longitudinal radiative slowing often does not help; near saturation, the two processes compete with each other, leading to a decrease in trappable beam brightness [13]. The maximum possible deceleration is $a_{\max} = h\Gamma/(2m\lambda)$, so large deceleration is achieved with low mass m, fast radiative decay rate Γ, and short wavelength λ. All three of these

factors favor MgF over current state-of-the-art CaF and YO experiments, with the expected trapping improved by as much as a factor of 7 or 20, respectively.

Laser slowing a MgF beam to a stop from an initial velocity of 150 m/s, typical of a cryogenic beam, requires optical cycling of a number of photons $N_\gamma \approx 6000$. At a minimum, a preliminary attempt to laser cool MgF requires knowledge of all vibrational branching fractions $b_{0v''} > 1/N_\gamma \approx 1.7 \times 10^{-4}$, as each corresponding ground vibrational state v'' will need to be addressed by a laser. Like other alkaline earth monofluorides, MgF is expected to have a nearly diagonal array of Franck-Condon factors, enabling laser cooling with few vibrational state repump lasers [14]. However, despite spectroscopic studies of MgF dating back nearly 100 years [15,16], we are not aware of any experimental determinations of vibrational branching at the 10^{-4} level. Moreover, while MgF is a relatively simple system where relativistic and correlation effects are minimal, predictions of the number of $b_{0v''} \gtrsim 10^{-4}$ are variously two [17,18], three [19], or four [20] in the literature. An accurate measurement of the vibrational branching fractions $b_{0v''}$ for MgF is therefore needed to inform the allocation of laser resources for laser cooling experiments, as well as to benchmark calculation methods for their applicability to more complicated laser coolable molecules. For example, branching fractions of order 10^{-5} can be predicted to within a factor of 2 even in triatomic molecules which contain heavy nuclei [21].

An upper limit on the spontaneous decay rate Γ of the MgF $A\,^2\Pi_{1/2}$ state was recently reported with approximately 4% fractional uncertainty in Ref. [22]. There, Γ was determined by measuring laser-induced fluorescence as a function of laser frequency and extrapolating the fitted Lorenzian linewidth to zero power. Several groups have performed calculations
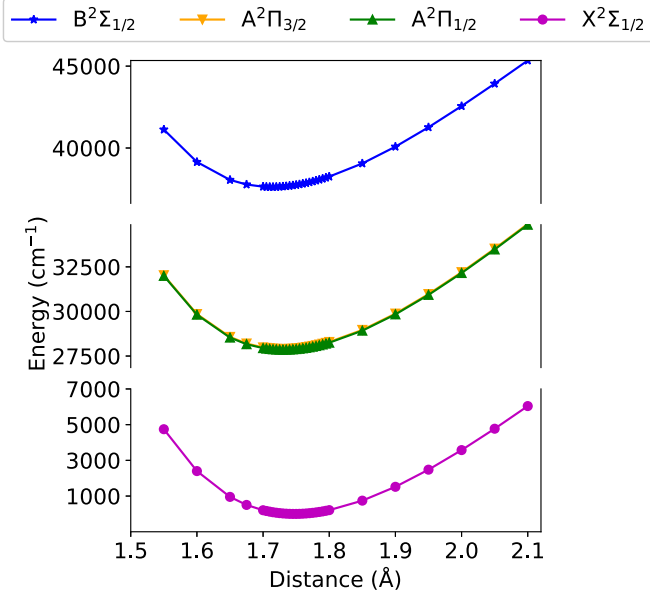
*eric.norrgard@nist.gov

FIG. 1. PECs for the ground and low-lying excited states of MgF obtained at 4c-FSCC(0,1) level and using the d-aug-dyall.ae4z basis set.

of Γ [17,20], roughly consistent with the measurement of Ref. [22].

Here we report measured values of radiative decay rates of the $A\,^2\Pi$ state and vibrational branching fractions of the $A\,^2\Pi_{1/2} \rightarrow X\,^2\Sigma^+$ transition in the MgF molecule. Branching fractions are measured by exciting the transition of relevance for laser cooling, which is $P_1(1)/Q_{12}(1)$ [23]. We find good agreement with theory, which is described in Sec. II. Our experimental results are detailed in Secs. III A and III B for the branching fractions and decay rates, respectively. Finally, we conclude with remarks in Sec. IV.

II. THEORY

A. Methodology

The $X\,^2\Sigma_{1/2}$ ground state and the $A\,^2\Pi_{1/2}$, $A\,^2\Pi_{3/2}$, and $B\,^2\Sigma_{1/2}$ excited states of the MgF molecule were investigated using the relativistic four-component Fock-space coupled-cluster method (4c-FSCC), including the Gaunt interaction. We initially solve the coupled-cluster equations for the closed-shell molecular ion, MgF$^+$. This serves as a reference for the subsequent FSCC(0,1) calculation of ground and excited states of the neutral MgF. The model space included four orbitals, needed to obtain the ground state and the excited states of interest. We employed the dyall.d-aug-ae4z [24] basis set and the default settings in the DIRAC23 program [25,26]. All electrons were correlated and the virtual space cutoff was set symmetric to energies of correlated electrons, which corresponds to 70 a.u.. These energies were corrected for the basis set superposition error (BSSE) and the truncation in the coupled-cluster expansion, as it is discussed in the Appendix A. We use the constructed potential energy curves (PECs) shown in Fig. 1 and the DUNHAM program [27] (written by Kellö, at the Comenius University) to calculate the spectroscopic constants, as defined by Herzberg [28]. T_e

represents the minimum on the electronic state PEC (relative to the ground state).

The transition rate between an upper $(n'v')$ and a lower $(n''v'')$ vibronic state, $\Gamma_{n'v'n''v''}$, is defined in terms of the transition dipole moment (TDM) function $M_{n'n''}(R)$ for the n' and n'' electronic states, and the transition frequency $\omega_{n'v'n''v''}$ between the $n'v'$ and $n''v''$ states

$$\Gamma_{n'v'n''v''} = \frac{\omega_{n'v'n''v''}^3}{3\pi\hbar\epsilon_0 c^3} |\langle v'|M(R)_{n'n''}|v''\rangle|^2, \tag{1}$$

where $\hbar$ is the reduced Planck constant and ϵ_0 the permittivity of the vacuum. In the r-centroid approximation [29], the above integral can be expressed as the product of the constant square of the TDM $M_{n'n''}^2$ and the square of the overlap of the vibrational wave functions, $q_{v'v''} = |\langle v'||v''\rangle|^2$, also called the Franck-Condon factors (FCFs),

$$\Gamma_{n'v'n''v''} = \frac{\omega_{n'v'n''v''}^3}{3\pi\hbar\epsilon_0 c^3} q_{v'v''} M_{n'n''}^2. \tag{2}$$

The decay rate $\Gamma_{n'v'}$ (or inverse of the lifetime $\tau_{n'v'}$) of an excited state $(n'v')$ may be expressed as the summation of Eq. (1) over all lower states $(n''v'')$

$$\Gamma_{n'v'} = \frac{1}{\tau_{n'v'}} = \sum_{n''v''} \Gamma_{n'v'n''v''}, \tag{3}$$

TDMs were obtained using the multireference configuration interactions level of theory (MRCI) in the MOLPRO program [30]. In the MRCI approach, we used the complete active space (9,9) reference allowing the single unpaired electron to occupy the Mg $3s$, $3p$, $4s$ orbitals and the F $2s$, $2p$ orbitals. The same basis set as the one employed for calculating the PECs, i.e. the dyall.d-aug-ae4z basis set [24], was used and all electrons were correlated. We calculate the TDMs using the MRCI method as this is not yet implemented in the FSCC method. To verify the validity of our approach, we compare the dipole moments calculated using FSCC and MRCI (see the discussion in Appendix B). We find no significant differences between the different methods and very good agreement with the experimental values when available. FCFs, decay rates, and lifetimes are calculated using the LEVEL16 program [31].

B. Results

Table I shows that the obtained spectroscopic constants are in a very good agreement with the previously reported experimental values. Furthermore, we use an equivalent approach to investigate the homologues of MgF, namely, CaF, SrF, and BaF [32]. For these heavier systems, the theoretical results were found to reproduce the experimental values very well, providing additional confirmation of the excellent performance of the selected computational method.

Figure 2 presents the FCFs $q_{v'v''}$ between vibrational levels up to $v = 5$ of the ground and excited states of MgF (the corresponding numerical values are collected in Table XI in the Appendix).

Table II presents the TDMs $M_{n'n''}$ for the first four electronic states of MgF.

The lifetimes are presented in Table III. There is very good agreement between the values determined by the full

TABLE I. Equilibrium bond lengths in Å and spectroscopic constants in cm^{-1} of the ground and the low-lying excited states of MgF obtained at the 4c-FSCC(0,1) level of theory and using the d-aug-dyall.ae4z basis set (including CP and ΔT corrections). *Constants calculated from the reported B_v and T_v values for $v = 0, 1$. $^\ddagger T_e$ values originally reported in Ref. [35] were equated with the band origins, and are thus corrected here using the other reported spectroscopic constants for the sake of consistency with the values in this work and Ref. [34]. †Obtained from the reported mean Λ-S state and the regular spin-orbit coupling.

	R_e	ω_e	$\omega_e\chi_e$	B_e	T_e	Ref.
$X\,^2\Sigma_{1/2}$	1.747	731.4	4.04	0.521		This work
	1.749937(1)	720.14042(30)	4.26018(16)	0.519272510(42)		[33]
	1.7500	721.6	4.94	0.51922		[34]*
$A\,^2\Pi_{1/2}$	1.730	761.2	4.11	0.531	27 856	This work
	1.7469	747.999(1)	4.274(5)	0.52106(6)	27 815.646(1)‡	[35]
	1.7470	746.6	3.25	0.52105	27 798.5†	[34]*
$A\,^2\Pi_{3/2}$	1.730	761.5	4.12	0.531	27 896	This work
	1.7212	748.097(6)	4.273(2)	0.53676(5)	27 852.005(5)‡	[35]
	1.7470	746.6	3.25	0.52105	27 834.9†	[34]*
$B\,^2\Sigma_{1/2}$	1.713	785.1	4.71	0.542	37 624	This work
	1.7185	762.2	5.63	0.53844	37 167.3	[34]*

R-dependent TDM calculation and the r-centroid approximation. Thus the r-centroid approximation (2) is easily applicable for this system in future studies. Decay rates are compared to the experiment later in the paper in Table VI.

The branching fractions $b_{v'v''}$ from a given excited state ($n'v'$) are expressed as

$$ b_{n'v'n''v''} = \frac{\Gamma_{n'v'n''v''}}{\Gamma_{n'v'}}. \tag{4} $$

In the r-centroid approximation, the branching fractions for the $A\,^2\Pi_{1/2}$ state are simply the FCFs renormalized with an $\omega_{n'v'n''v''}^3$ weighting. Branching fractions are compared to the experiment later in the paper in Table IV.

In the remainder of this work, we consider only transitions between the $A\,^2\Pi$ and $X\,^2\Sigma^+$ states, and the labels n' and n'' are left out for simplicity of notation.
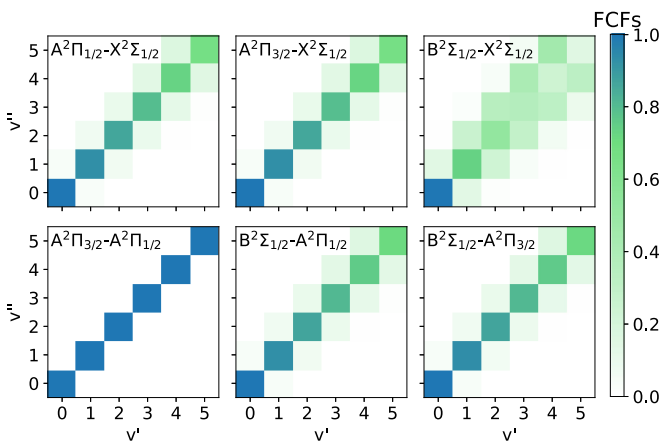

FIG. 2. FCFs for the vibronic transitions between the upper (v') and lower (v'') electronic states. Table XI in Appendix C presents the corresponding numerical values.

III. EXPERIMENT

Experimental data were collected in the same apparatus used in a recent measurement of the decay rates of the Cr $y^7P^\circ_{2,3,4}$ states [36]. A cryogenic buffer gas beam (CBGB) of MgF is produced by laser ablation of a sintered MgF_2 precursor target. We orient our experiment by taking $\hat{z}$ to be the direction of travel of the molecular beam (roughly horizontal), $\hat{y}$ vertically upward, and $\hat{x}$ parallel to the ground and forming a right-handed coordinate system.

The molecular beam is excited by a nominal 15 mm 1/e^2 diameter laser beam which is retroreflected such that it propagates in the $\pm\hat{y}$ directions. The laser is typically polarized linearly in the $\hat{z}$ direction. The light is produced using a frequency-doubled titanium-doped sapphire laser. For decay rate measurements, the light is pulsed on and off using an acoustooptic modulator (AOM). The AOM's first-order diffracted beam is directed to the molecular beam vacuum chamber via a 1-m-long polarization maintaining optical fiber.

Fluorescence is collected along the $\pm\hat{x}$ axes by two identical imaging systems. Each imaging system consists of a broadband antireflection coated fused silica vacuum viewport, a 75-mm focal length planoconvex singlet lens placed one focal length away from the center of the chamber, and a camera lens assembly focused to infinity. To select fluorescence from a particular vibronic transition, one or more interference

TABLE II. Calculated transition dipole moments (in ea_0, where e is the electron charge and a_0 is the Bohr radius) for the ground-state bond length (1.747 Å) using the SO-MRCI method and the d-aug-dyall.ae4z basis set.

Transition	TDM
$A\,^2\Pi_{1/2}$–$X\,^2\Sigma_{1/2}$	1.802
$A\,^2\Pi_{3/2}$–$X\,^2\Sigma_{1/2}$	1.802
$B\,^2\Sigma_{1/2}$–$X\,^2\Sigma_{1/2}$	1.492
$A\,^2\Pi_{3/2}$–$A\,^2\Pi_{1/2}$	0.001
$B\,^2\Sigma_{1/2}$–$A\,^2\Pi_{1/2}$	0.504
$B\,^2\Sigma_{1/2}$–$A\,^2\Pi_{3/2}$	0.504

TABLE III. Lifetimes in ns for the electronic excited states of MgF calculated using the simplified r-centroid approximation, Eq. (2), and the full R-dependent TDM, Eq. (1).

State	τ [Eq. (2)]	τ [Eq. (1)]
$A\,^2\Pi_{1/2}$	7.04	7.03
$A\,^2\Pi_{3/2}$	7.01	7.00
$B\,^2\Sigma_{1/2}$	4.17	4.12

filters are placed between the singlet lens and camera lens assembly. To minimize angle-of-incidence-dependent transmission through the filters, the possible angles of incidence on the filters are restricted to $\theta < 7°$ by placing two 18-mm diameter apertures spaced by 150 mm between the singlet lens and the filters. Photons are detected using photomultipliers (PMTs) and counted using a multichannel event timer with 80-ps timing resolution. For fluorescence lifetime measurements, a hybrid PMT-avalanche photodiode is used to remove afterpulsing systematic effects [37]. Timing, computer control of equipment, and data collection are performed using the LABSCRIPT SUITE [38].

The MgF$_2$ target is ablated using a 10-ns-long pulse of 532-nm light. Pulse energies between 25 mJ and 50 mJ were found to produce the best yield. The source is run with a He buffer gas flow rate of 7×10^5 Pa mL/min, or 7 standard cubic centimeters per minute. Compared to Cr [36] or sintered SrF$_2$ [39] precursor targets, the yield from sintered MgF$_2$ precursor targets decays rapidly, dropping by roughly half after typically 100 ablation pulses. This has motivated us to begin construction of a CBGB based on the chemical reaction between the Mg metal and a fluorinated gas [22,40], which should stably produce high yields.

A. Branching fractions

In this section we detail the measurement of the branching fractions $b_{0v''}$ from the ^{24}MgF $|A\,^2\Pi_{1/2}, v' = 0; J' = 1/2, P' = +\rangle$ state (that is, the excited state typically used in laser cooling applications) to ground vibrational levels v'' by measuring laser-induced fluorescence at transition wavelength $\lambda_{0v''}$. Table IV summarizes the experimental results and our calculated values derived from weighting the Franck-Condon factors $q_{0v''}$ of Sec. II by applying Eq. (4).

Our branching-fraction measurement procedure is based on the one used in the Amherst College group's investigation of TlF [41,42]. Two different bandpass interference filters i and j are inserted into the imaging systems 1 and 2 to simultaneously monitor two vibronic transitions at wavelengths λ_{0i} and λ_{0j}, respectively. The multichannel event timer stores the detected photon counts from both detectors in a histogram of 2.6-μs time bins. The counts in a 5-ms interval between ablation pulses are used to determine the mean background counts per bin. The background is subtracted from a 1.6-ms signal interval, which roughly corresponds to the full width at half maximum of the fluorescence signal, to determine the number of fluorescence counts. The uncertainty in the number of fluorescence counts, listed as "statistical uncertainty" in Table IV, is determined by the uncorrelated combination of

the uncertainty in the signal counts and the uncertainty in the background counts, assuming shot noise.

We observed fluorescence on all vibronic bands up to $v'' = 3$. An unsuccessful attempt was made to detect fluorescence at wavelength λ_{04}, which set an experimental upper limit of roughly three times the calculated value for b_{04}.

The fluorescence counts on detector a with filter i is

$$S_i^{(a)} = N b_{0i} f_i \eta_i^{(a)}, \qquad (5)$$

where f_i is the transmission efficiency of the filter, $\eta_i^{(a)}$ is the combined geometric and quantum efficiency for detector a at wavelength λ_{0i}, and N is the total number of molecules excited by the laser. In each run of the branching-fraction experiment, we take the ratio $r_{ij} = S_i^{(1)}/S_j^{(2)}$ of the two signals. The experiment is then repeated with the filters swapped to obtain the signal ratio r_{ji}. Comparing these two measurements yields the ratio of branching fractions

$$\frac{b_{0i}}{b_{0j}} = \frac{f_j}{f_i} \sqrt{\frac{\eta_j^{(2)}\eta_j^{(1)}}{\eta_i^{(1)}\eta_i^{(2)}}} \sqrt{\frac{r_{ij}}{r_{ji}}}. \qquad (6)$$

A sufficient number of ratio measurements were taken to overconstrain a fit to the branching fractions $b_{0v''}$. For example, we may derive the ratio b_{03}/b_{00} by either comparing the $i = 0, 3$ data only

$$\frac{b_{03}}{b_{00}} = \frac{f_0}{f_3} \sqrt{\frac{\eta_0^{(1)}\eta_0^{(2)}}{\eta_3^{(1)}\eta_3^{(2)}}} \sqrt{\frac{r_{30}}{r_{03}}}, \qquad (7)$$

or by comparing the $i = 0, 1, 3$ data

$$\frac{b_{03}}{b_{00}} = \frac{f_0}{f_3} \sqrt{\frac{\eta_0^{(1)}\eta_0^{(2)}}{\eta_3^{(2)}\eta_3^{(1)}}} \sqrt{\frac{r_{31}}{r_{13}}\frac{r_{10}}{r_{01}}}. \qquad (8)$$

The two methods are statistically consistent for the ratio b_{03}/b_{00}, and the weighted mean of these two determinations is used in the analysis. However, repeating the similar procedure for the ratio b_{02}/b_{00}, we find a 3-σ discrepancy between comparisons of the $i = 0, 2$ data and the $i = 0, 1, 2$ data. We take the mean of these two determinations as the reported ratio b_{02}/b_{00}, and the difference of the two determinations as the uncertainty in this ratio. The impact of this additional uncertainty on the branching fractions $b_{0v''}$ is labeled as "Normalization discrepancy" in Table IV.

To achieve the lowest possible uncertainty branching-fraction measurements, it was necessary to accurately characterize the light-collection efficiency of our imaging system as well as the transmission properties of the bandpass interference filters. The response of the entire imaging system was compared to the response of a calibrated photodiode as a function of wavelength in the National Institute of Standards and Technology (NIST) Detector Calibration Facility [43]. Spectral responsivity calibration uncertainties as low as 0.005% are possible in this facility.

The Detector Calibration Facility operating principle is to use a quartz-tungsten-halogen lamp filtered by a prism-grating monochromator to provide a low-noise, wavelength-tunable light source. For our calibration, the 75-mm focal length lens was adjusted to provide a well-collimated beam of light beyond the relay-mirror assembly of the monochromator. To

TABLE IV. Branching fractions $b_{0v''}$ and 1σ error budget for the MgF $A\,^2\Pi_{1/2}$ state.

Parameter	b_{00}	b_{01}	b_{02}	b_{03}	b_{04+}
Branching fraction-theory	0.965 8	0.033 2	0.000 93	0.000 025	0.000 001
Branching fraction-measured	0.967 63	0.031 42	0.000 91	0.000 044	<0.000 02
Total uncertainty	0.000 28	0.000 27	0.000 03	0.000 013	
Statistical uncertainty	0.000 08	0.000 08	0.000 01	0.000 013	
Systematic uncertainties:					
Normalization discrepancy	0.000 03	0.000 00	0.000 03	0.000 000	
Calibration-statistical	0.000 02	0.000 02	0.000 001	0.000 000	
Calibration-power drift	0.000 12	0.000 12	0.000 004	0.000 000	
Filter transmission	0.000 18	0.000 18	0.000 00	0.000 000	
Total systematic uncertainty	0.000 27	0.000 16	0.000 004	0.000 000	

reduce the light intensity to below the saturation threshold of the PMTs, two neutral density filters were inserted into the optical beam path of the NIST Detector Calibration Facility. The transmission of each filter was calibrated separately and the uncertainties are accounted for in the final detection efficiency measurement. Calibration data were recorded for a few minutes for each setting, until the statistical uncertainty in the response was approximately 0.1%.

To ensure the calibration was insensitive to the alignment of the light into the imaging system, an iris was placed in front of the first neutral density filter and adjusted so that the beam size at the PMT was smaller than the active detection area of the PMTs. This was confirmed by placing the PMT in a position where there was no change in the observed signal with displacement in either the horizontal and vertical directions. The optical power was measured with a calibrated photodiode before and after the calibration of each PMT to account for drifts in the optical power.

For each detector and filter combination $i \neq 0$, we perform absolute photon collection efficiency calibrations at the filter's vibronic pass band λ_{0i} as well as λ_{00}. For filter $i = 0$ we calibrated each detector at λ_{00} and λ_{01}. The transmission is $<10^{-3}$ for all other wavelength and filter combinations, contributing negligibly to the error estimate. This allows for all molecule fluorescence signals to be corrected for the small amount of λ_{0j} ($j \neq i$) light transmitted by filter i. This correction is approximately 10% for ratios involving $v'' = 3$, and less than 1.4% for all stronger transitions.

The dependence of the filter transmission on wavelength and angle of incidence was measured in the NIST facility for Regular Spectral Transmittance [44]. The error due to the collection of light at nonzero angles of incidence is estimated by comparing the results of several Zemax [45] ray-tracing simulations. The simulations are designed to realistically model the collection optics. The simulation includes the full optical system less the vacuum viewport. A 15-mm diameter, 100-mm-long cylindrical light source (uniform probability for emission of a light ray in both position and direction) oriented perpendicular to the optical collection axis is used to model the overlap of the excitation laser with the molecular beam.

From these simulations, the probability for a photon to reach the detector with a given angle of incidence is determined. This calculated collection efficiency is weighted by the measured angle-dependent filter transmission. The

angle-dependent transmission uncertainty is estimated as the difference between the calculated transmission for all light at normal incidence and the calculated transmission of our more realistic simulation. The angle-dependent uncertainty on the transmission is 5% for the $i = 3$ filter, which is well below the 30% fractional statistical uncertainty for this weak transition. All other filters were determined to have less than 0.3% angle-dependent uncertainty. All filters are also assigned a 0.5% transmission uncertainty from their calibration at the NIST facility for Regular Spectral Transmittance. Simulations with individual optical components displaced by 3 mm were found to change the calculated transmission by, at most, one order of magnitude less than the estimated angle-dependent transmission uncertainty.

B. Decay rates

In this section, we detail the measurement and analysis procedures used to determine the spontaneous decay rates Γ. Our measured values of Γ for the $A\,^2\Pi_{1/2}$ and $A\,^2\Pi_{3/2}$ states are presented in Table V with a list of uncertainty estimates. Our analysis procedure closely follows that of Ref. [36].

TABLE V. Measured decay rates Γ and 1σ error budget for the MgF $A\,^2\Pi$ states.

Parameter ($\times 10^6\,\text{s}^{-1}$)	$A\,^2\Pi_{1/2}$	$A\,^2\Pi_{3/2}$
Decay rate Γ	131.6	129.5
Total uncertainty	1.4	0.9
Statistical uncertainty	0.9	0.8
Systematic uncertainties:		
Truncation error	0.26	0.24
Quantum beats		
Laser detuning	1.1	0.17
Laser polarization	0.04	0.15
$\mathcal{B}_x$	0.03	0.15
$\mathcal{B}_y$	0.04	0.03
$\mathcal{B}_z$	0.04	0.04
Pulse pileup	0.005	0.007
Differential nonlinearity	0.014	0.014
Time calibration	0.003	0.003
Total systematic uncertainty	1.1	0.4

All data for the $A\,^2\Pi_{1/2}$ state are collected with the laser tuned to the $P_1(1)/Q_{12}(1)$ laser cooling transition. Because the $A\,^2\Pi_{3/2}$ state is typically not used for laser cooling, there is no obvious preferred rotational line to investigate. The MgF beam is observed to have the highest population in the $N = 3$ rotational state; therefore all data for the $A\,^2\Pi_{3/2}$ state are taken with the laser tuned to the $R_2(3)/Q_{21}(3)$ line. Typical laser power for the decay rate measurements is 40 mW. To minimize background-scattered laser light, fluorescence is monitored on the decay to $v'' = 1$ using the $\lambda_{01} = 368.4\,\text{nm}$ interference filter.

In the standard measurement configuration, the AOM produces 1.8×10^4 light pulses per ablation pulse. The light pulses have a full width at half maximum of 16 ns and a pulse repetition rate of 6 MHz. The MgF target is ablated at a repetition rate of 2 Hz. A histogram of events is collected with 80 ps time bins by the event timer with data readout performed after 300 ablation pulses. The procedure is then repeated, absent the ablation pulse, to obtain a background-scattered light signal. This signal plus background measurement procedure is repeated until the desired 1% to 2% statistical uncertainty on the decay rate is achieved, with the cumulative data constituting an experimental "run." A single run lasts roughly 40 min. We performed ten runs measuring the decay rate of the $A\,^2\Pi_{1/2}$ and six runs measuring the $A\,^2\Pi_{3/2}$. Our reported values for the decay rates in Table V are the weighted means of all runs for each state. In addition, several runs were performed on each state with one experimental parameter varied to quantify potential systematic errors.

1. Pulse pileup

We account for missed counts due to coincident events, or "pulse pileup," by following the procedure outlined in Ref. [36]. Decay rate data are typically collected at a rate of roughly 1 count per 1000 excitation cycles. The multihit-capable event timer has a dead time of 650 ps, and the photodetector has a maximum average count rate of 80 MHz. We correct the raw signal counts N_i in each time bin i to obtain N_i' corrected counts per time bin using

$$N_i' = \frac{N_i}{1 - \frac{1}{N_{\text{cycle}}}\sum_{j=i-k_d}^{i} N_j}, \qquad (9)$$

where N_{cylcle} is the total number of excitation cycles and $k_d = t_{\text{bin}} \times 80\,\text{MHz}$ is the number of time bins of width t_{bin} in the detector-limited deadtime [46]. We estimate the error $\delta\Gamma$ due to this correction by analyzing the data assuming the detector has no response after the first detection of an excitation cycle. The difference is less than 5×10^{-5} fractional uncertainty $\delta\Gamma/\Gamma$ for our measurements.

2. Fit procedure and truncation error

After correcting for pulse pileup, background counts $N_i^{\text{bg}'}$ are subtracted from the signal counts $N_i^{\text{sig}'}$. The resulting data are binned in 800-ps intervals and fit to a single decaying exponential

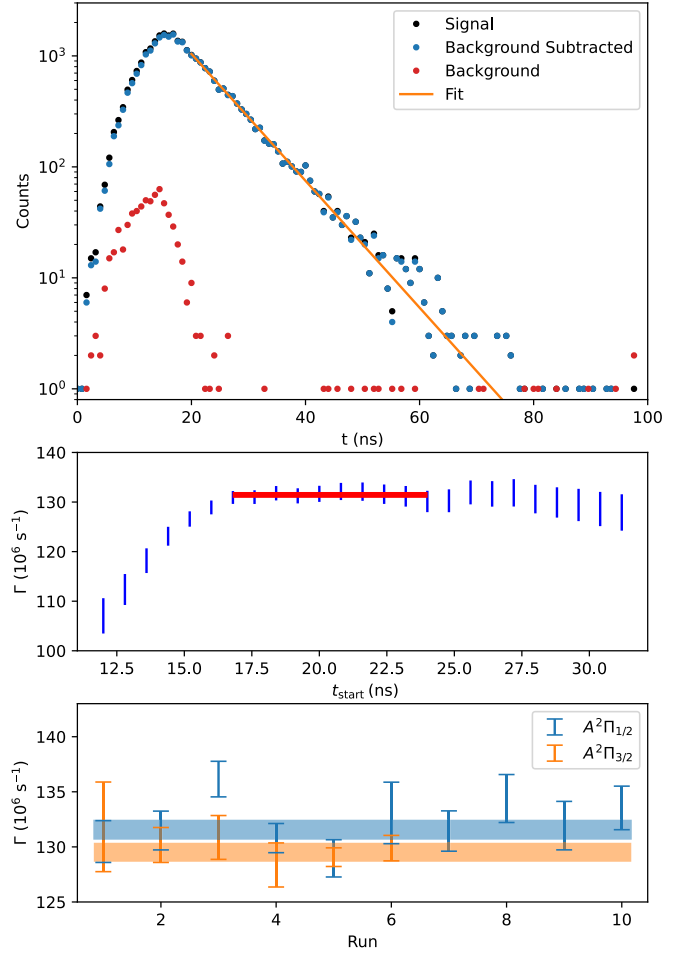$$N_i^{\text{sig}'} - N_i^{\text{bg}'} = Ae^{-\Gamma t_i}. \qquad (10)$$

FIG. 3. (Top) Histogram of counts as a function of time for a typical run (number 7) to determine decay rate Γ for the $A\,^2\Pi_{1/2}$ state. The histogram bin width is 800 ps. The line labeled "fit" is a representative fit to Eq. (10) with $t_{\text{start}} = 20\,\text{ns}$. (Middle) Fitted Γ as a function of t_{start} (blue line) for a typical run (number 7). Error bars denote the fit uncertainty at each t_{start}. The range of t_{start} chosen for our analysis and the standard deviation of fitted Γ over this range are indicated by the range and thickness red line, respectively. (Bottom) Data points are the fitted Γ for each run. Error bars are the quadrature sum of fit and truncation uncertainties. Shaded bands denote the 1σ uncertainty band obtained by a weighted average of all runs for each excited state.

When a constant offset was added to Eq. (10), the offset was found to be statistically consistent with zero and did not change the fitted decay rate within its statistical uncertainty. Pulse-pileup-corrected data for a typical experimental run measuring the $A\,^2\Pi_{1/2}$ decay rate are shown in upper panel of Fig. 3.

The arbitrary choice of the start time t_{start} of the fit may influence the decay-rate measurement (sometimes called truncation error). We vary t_{start}, setting this parameter to the start of each $t_{\text{bin}} = 800\,\text{ps}$ time bin over a 7-ns range, which corresponds to between about 50% to 20% of the peak observed counts (Fig. 3 middle panel). For each run, we assign a value for Γ by taking the average fitted Γ over this 7-ns range of start times, weighted by the nonlinear least-squares 1σ confidence interval when fitting to Eq. (10). We assign a statistical

uncertainty equal to the median 1σ nonlinear least-squares fit uncertainty in the range, and assign a truncation uncertainty equal to the standard deviation of the fitted Γ values.

The assigned decay rate Γ and the combined statistical and truncation uncertainties for each run are shown in the bottom panel of Fig. 3. The shaded bands depict the weighted average and standard error of all runs for each state. The calculations of Sec. II predict the $A\,^2\Pi_{3/2}$ decay rate to be 6×10^5 s^{-1} faster than the $A\,^2\Pi_{1/2}$ decay rate, that is, equal within the statistical sensitivity of our measurement. Indeed, accounting for all sources of uncertainty detailed below, we find no statistically significant difference in the decay rates MgF $A\,^2\Pi_{1/2}$ [$\Gamma = 1.316(14) \times 10^8$ s^{-1}] and $A\,^2\Pi_{3/2}$ [$\Gamma = 1.295(9) \times 10^8$ s^{-1}] states.

3. Quantum beats

In addition to the exponential decay expected in Eq. (10), an oscillatory amplitude may be observed due to hyperfine and Zeeman quantum beats. The laser pulse has a full width at half maximum of 16 ns, corresponding to a Fourier-limited linewidth of about $2\pi \times 100$ MHz. For the $A\,^2\Pi_{1/2}$ decay rate measurement, the laser is typically tuned to the peak in fluorescence around the unresolved $|X\,^2\Sigma^+; N = 1, J = 3/2, F = 1, 2, P = -\rangle \rightarrow |A\,^2\Pi_{1/2}; J' = 1/2, F' = 0, 1, P' = +\rangle$ transitions. For these transitions, electric dipole selection rules restrict all ground states to being excited to one or the other excited state $F' = 0, 1$ manifold, but not both. Therefore, hyperfine quantum beats should not be observed in the $A\,^2\Pi_{1/2}$. For the $A\,^2\Pi_{3/2}$ decay-rate measurement, the partially resolved $|X\,^2\Sigma^+; N = 3, J = 7/2, F = 3, 4, P = -\rangle \rightarrow |A\,^2\Pi_{3/2}; J' = 7/2, F' = 3, 4, P' = +\rangle$ transitions are excited. The $F' = 3, 4$ levels are separated in energy by about $\Delta E/\hbar = 2\pi \times 31$ MHz [22], and therefore, we may expect to see evidence of hyperfine quantum beats in the $R_2(3)/Q_{21}(3)$ signal.

We test for systematic errors due to hyperfine quantum beats by attempting to preferentially excite of one or the other excited-state hyperfine level by varying the laser detuning by $+20$ MHz and -20 MHz from the fluorescence peak. We find a statistical difference in the fitted Γ when detuning the laser for the $A\,^2\Pi_{1/2}$ level; the uncertainty obtained by linear regression is $\delta\Gamma/\Gamma = 0.8\%$ for this level. As this was within our target accuracy, the effect was not investigated further. The uncertainty due to laser detuning on the $A\,^2\Pi_{3/2}$ decay rate is roughly one order of magnitude smaller.

Possible systematic error due to Zeeman quantum beats is substantially mitigated compared to our recent Cr decay-rate measurements [36] by improved control of the magnetic field. Three pairs of Helmholtz coils surround the interaction region of the experiment. Using the Helmholtz coils and a three-axis Hall sensor, we map out the small field hysteresis loop of the vacuum chamber such that we may set the residual magnetization in a deterministic way. We then apply a bias field to either null the residual magnetization for standard data, or apply a known magnetic field of up to 0.2 mT along each axis to exaggerate the effects of uncancelled magnetic fields. We estimate the uncertainty in the nulled magnetic field to be 8 μT.

For the $A\,^2\Pi_{1/2}$ state, the g factor is expected to be small ($g < 0.01$), and thus Zeeman quantum beats should be

TABLE VI. Comparison of our measured and calculated decay rates to values from previous works. Values in parentheses are the combined 1σ statistical and systematic uncertainty.

Method	Decay rate $\Gamma(\times 10^6$ s$^{-1})$		Ref.
	$A\,^2\Pi_{1/2}$	$A\,^2\Pi_{3/2}$	
Experiment	131.6(1.4)	129.5(9)	This work
Theory	142.3	142.9	This work
Experiment	138(7)	—	[22]
Experiment	138(7)	—	[22]
Theory	—	139.6	—	[17]
Theory	—	125.6	—	[20]

negligible even for the largest 0.2-mT magnetic fields applied. Indeed, no statistically significant magnetic field effect on Γ is observed for this state. Regardless of the magnitude of the g factor, our experimental geometry (excitation light polarized along $\hat{z}$ and imaging along $\hat{x}$), should preclude observing Zeeman quantum beats for applied $\mathcal{B}_x$ or $\mathcal{B}_z$. We observe no statistically significant effect in these cases for the $A\,^2\Pi_{3/2}$, though a relatively poor constraint on the effect of uncanceled $\mathcal{B}_x$ was obtained due to a smaller number of measurements taken. It should be possible to observe Zeeman quantum beats for an applied $\mathcal{B}_y$ field, and an attempt was made to assign a g factor to the $A\,^2\Pi_{3/2}$ state by applying a large bias field $\mathcal{B}_y = 2$ mT. While the fitted Γ under these conditions increased to $1.38(3) \times 10^8$ s^{-1}, the contrast was too poor to reliably fit an oscillatory term and assign a g factor. For all cases, the fractional uncertainty due to uncanceled magnetic fields is $\delta\Gamma/\Gamma < 0.12\%$.

Finally, we tested for the effect of laser polarization on possible quantum beats by exciting with light linearly polarized along $\hat{x}$ instead of along $\hat{z}$. For zero magnetic field, we expect the laser polarization to have no effect. A statistically significant deviation in the decay rate was observed for the $A\,^2\Pi_{3/2}$ level leading to a fractional uncertainty of $\delta\Gamma/\Gamma = 0.15\%$. Again, this effect was sufficiently small that it was not further investigated. No statistically significant shift was observed for the $A\,^2\Pi_{1/2}$ level.

4. Time calibration

Uncertainties due to differential nonlinearity (that is, noncumulative uncertainty in the bin width of the event timer) and time calibration of the event timer are assigned in an identical manner to that described in our Cr decay-rate measurement [36]. The uncertainty due to these effects is at least several times smaller than the other sources of uncertainty considered above.

IV. COMPARISON OF RESULTS AND CONCLUSIONS

Table VI compares the experimental and calculated decay rates of the $A\,^2\Pi$ state determined in this work with values reported elsewhere.

By using a calibrated imaging system, we have determined the vibrational branching fractions of MgF to an unprecedented accuracy. This sets a precision benchmark for vibrational branching calculations, and we find excellent
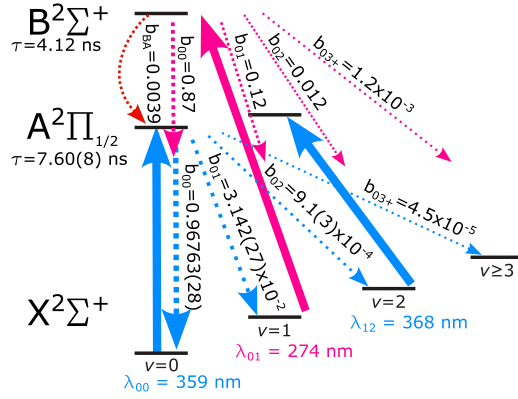
FIG. 4. Possible optical cycling scheme for MgF. Blue, pink, and red arrows denote X-A, X-B, and A-B transitions, respectively. Solid lines denote laser excitation. Dashed lines denote radiative decay. Values without uncertainties are calculated.

TABLE VII. Effect of the quality of the basis set on the energies relative to the $X\,^2\Sigma_{1/2}$ ground state in cm^{-1} at 1.75 Å and including a cutoff of -70 a.u. to 70 a.u.

Basis	$A\,^2\Pi_{1/2}$	$A\,^2\Pi_{3/2}$	$B\,^2\Sigma_{1/2}$
dyall.v3z	28 573.5	28 616.6	39 837.9
dyall.v4z	28 235.5	28 277.2	38 813.5
dyall.ae4z	28 235.4	28 277.1	38 813.6
dyall.s-aug-ae4z	27 848.1	27 887.5	37 548.0
dyall.d-aug-ae4z	27 834.9	27 874.2	37 429.9
dyall.t-aug-ae4z	27 834.8	27 874.1	37 429.3

agreement with values calculated using multireference relativistic Fock-space coupled-cluster method (within 0.2% for b_{00}, Table IV). Given this near-perfect match confirming the accuracy of the calculated FCFs as well as a very good agreement in transition energies (the theoretical T_e values agree within 0.2% with the experiment, Table I), the observed overshooting of theoretical decay rates (Table VI) can be almost entirely attributed to the uncertainty in the calculated TDM values.

The radiative decay rate and vibrational branching fractions for the MgF $A\,^2\Pi_{1/2}$ state are highly favorable for laser cooling. With three lasers addressing $A \leftarrow X$ transitions, it should be possible to scatter up to $1/b_{03} \approx 2 \times 10^4$ photons with a maximum possible scattering rate of $R_{\rm sc}^{\rm max} = \Gamma/7$ [47–49]. Another possible optical cycling scheme is depicted Fig. 4. By repumping the $v'' = 1$ level through the $B\,^2\Sigma^+$ state instead of the $A\,^2\Pi_{1/2}$ state, this scheme avoids producing a Λ system between the main cycling laser (wavelength λ_{00}) and first repump laser (wavelength λ_{01}) [49]; the maximum possible scattering rate is then $R_{\rm sc}^{\rm max} = \Gamma/4$. This comes at the cost of an additional loss channel due to $B \to A$ decays, with roughly $b_{01}b_{\rm BA} = 1.2 \times 10^{-4}$ probability per optical cycle. Molecules will subsequently decay to the $|X\,^2\Sigma^+, v'' = 0; N'' = 0, 2\rangle$ levels. The states could be repumped by driving $N'' = 0 \leftrightarrow N'' = 1 \leftrightarrow N'' = 2$ microwave transitions ($R_{\rm sc}^{\rm max} = \Gamma/10$), or by a combination of $N'' = 0 \leftrightarrow N'' = 1$ microwaves and an $N'' = 2$ repump laser ($R_{\rm sc}^{\rm max} = \Gamma/5$) [48]. The $B \to A$ transitions also have highly diagonal FCFs (see Table XI in the Appendix), allowing $>2 \times 10^5$ photon scatters before additional rovibrational losses via this channel; rotational repumping in excited vibrational states via microwave is straightforward.

While the maximum possible scattering rate for the scheme depicted in Fig. 4 is $R_{\rm sc}^{\rm max} = \Gamma/4$, using the PYLCP PYTHON package [50] to simulate a magneto-optical trap (MOT) with realistic parameters, we find that the maximum rate of decelerating photon scatters is typically closer to $R_{\rm sc} \approx \Gamma/20$. Nonetheless, this photon scattering rate is sufficient to stop molecules with initial velocities up to 100 m/s in a distance of only 3 cm. This small stopping distance suggests it may be possible to directly load a MgF MOT from a CBGB source

without additional slowing mechanisms [51], which would enable the loading of multiple molecule pulses from the CBGB [52]. Details of these simulations are explored in a related work [53].

APPENDIX A: POTENTIAL ENERGY CURVES

To evaluate the robustness of our calculated results, we study the effect of the basis set [convergence and basis set superposition error (BSSE)], Gaunt Hamiltonian, correlation (truncation of the coupled-cluster expansion), on the $X\,^2\Sigma_{1/2}$ ground-state and the $A\,^2\Pi_{1/2}$, $A\,^2\Pi_{3/2}$, and $B\,^2\Sigma_{1/2}$ excited states energies of the MgF molecule. We included the Gaunt term in the 4c-FSCC final calculations and it is presented here only for completeness. The effect of the truncation in the coupled-cluster expansion was evaluated by calculating the CCSDT energies at the FSCC(0,1) level of theory using the dyall.v3z basis set and a cutoff from -10 a.u. to 20 a.u. in the EXP-T program [54,55]. Finally, BSSE of the used d-aug-dyall.ae4z basis set was corrected for using the usual counterpoise (CP) correction [56] at the 4c-FSCC(0,1) level of theory in DIRAC with Mg$^+$ and F$^-$ atomic fragments (given the ionic nature of the bond).

The CP and ΔT corrections in all the studied electronic states of MgF depend quadratically on the bond distance. We used a quadratic fitting for each effect and electronic state separately (see Fig. 5) and used these fitted curves to correct the final PECs. Table VIII presents the obtained spectroscopic constants. Additionally, to estimate the uncertainty due to the incompleteness of the basis set, which is the largest source of uncertainty (see Table VII), we calculate the spectroscopic constants with the energies obtained using the dyall.d-aug.ae3z basis set while keeping all the other parameters constants. By taking $\sqrt{(X_{\rm final} - X_{\rm uncorrected})^2 + (X_{\rm 4z} - X_{\rm 3z})^2}$
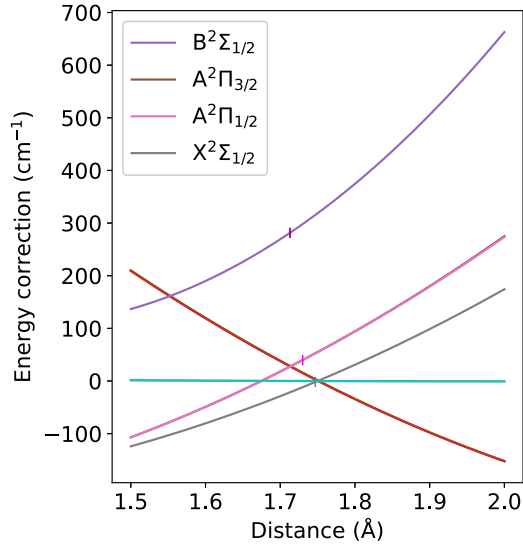
FIG. 5. Quadratic fitting for the effect of the triple excitations in the coupled cluster expansion (positive slope) and for the counterpoise correction (negative slope). In the CP correction, no visual distinction can be made for the different states, therefore, we omit the labels. Also the DBOC corrections for the ground state are presented (flat teal line). The vertical notches represent the equilibrium bond length of the corresponding state.

for each property X, we found all the parameters differ in no more than 1.4%, except $\omega_e \chi_e$ which changes up to 6.1% for the B state and up to 3.7% for the other states. Importantly, the effect on the final lifetimes is even smaller compared to the effect on the individual spectroscopic constants, with only 0.6% for the A state and 2.5% for the B state. The remaining higher-order correlation and basis-set incompleteness errors are expected to be significantly smaller than the evaluated errors given the typical convergence of the spectroscopic parameters with the excitation order and basis set cardinality. We evaluated the effects of diagonal Born-Oppenheimer

TABLE VIII. Equilibrium bond lengths in Å, spectroscopic constants in cm^{-1}, and lifetimes in ns of the ground and the low-lying excited states of MgF obtained at the 4c-FSCC(0,1) level of theory and using the d-aug-dyall.ae3z basis set (3z), the d-aug-dyall.ae4z basis set (4z), and the d-aug-dyall.ae4z + BSSE + triples excitations effect (final).

	Method	R_e	ω_e	$\omega_e \chi_e$	B_e	T_e	τ
$X\,^2\Sigma_{1/2}$	Final	1.747	731.4	4.04	0.521		
	4z	1.747	729.3	4.17	0.521		
	3z	1.750	724.0	4.12	0.519		
$A\,^2\Pi_{1/2}$	final	1.730	761.2	4.11	0.531	27 856	7.03
	4z	1.730	757.5	4.26	0.531	27 802	7.07
	3z	1.733	751.7	4.21	0.529	27 788	7.09
$A\,^2\Pi_{3/2}$	Final	1.730	761.5	4.12	0.531	27 896	7.00
	4z	1.730	757.6	4.25	0.531	27 841	7.04
	3z	1.733	751.8	4.21	0.529	27 827	7.06
$B\,^2\Sigma_{1/2}$	Final	1.713	785.1	4.71	0.542	37 624	4.12
	4z	1.714	775.7	4.99	0.541	37 315	4.22
	3z	1.717	770.0	4.93	0.540	37 295	4.23

TABLE IX. Transition (top) and permanent (below) dipole moments in ea_0 at the ground-state bond length calculated using the MRCI and FSCC methods. Experimental values obtained from Ref. [22].

Transition or state	MRCI MOLPRO	MRCI DIRAC	FSCC DIRAC	Expt.
$A\,^2\Pi_{1/2}$–$X\,^2\Sigma_{1/2}$	1.837	1.798		
$A\,^2\Pi_{3/2}$–$X\,^2\Sigma_{1/2}$	1.837	1.798		
$B\,^2\Sigma_{1/2}$–$X\,^2\Sigma_{1/2}$	1.499	1.507		
$A\,^2\Pi_{3/2}$–$A\,^2\Pi_{1/2}$	0.001	0.003		
$B\,^2\Sigma_{1/2}$–$A\,^2\Pi_{1/2}$	0.332	0.310		
$B\,^2\Sigma_{1/2}$–$A\,^2\Pi_{3/2}$	0.332	0.310		
$X\,^2\Sigma_{1/2}$	1.220	1.210	1.233	1.13(8)
$A\,^2\Pi_{1/2}$	1.398	1.365	1.399	1.26(9)
$A\,^2\Pi_{3/2}$	1.398	1.362	1.396	1.26(9)
$B\,^2\Sigma_{1/2}$	0.265	0.270	0.225	

corrections (DBOC); these are negligible, as can be seen in Fig. 5. We did not perform an explicit calculation of the effect of quantum electrodynamics (QED) contributions. However, these were recently presented for a set of heavier molecules [57]; these were estimated to be 1 to 2 orders of magnitude smaller compared to the CP and ΔT corrections presented here and we can thus safely neglect them.

APPENDIX B: DIPOLE MOMENTS

We compare the PDMs calculated with the MRCI and the FSCC methods. Furthermore, to validate the switch from one computational toolbox to another, we compare the TDMs and PDMs calculated with the DIRAC [58] and MOLPRO programs (using the MRCI approach). In all the cases, we use the d-aug-dyall.ae4z basis set, and we freeze four electrons. In the calculations carried out with MRCI and FSCC methods using the DIRAC program, we include in the correlation description all the virtual orbitals up to 5 a.u. and 10 a.u., respectively, and we used a two-component relativistic formalism (X2C). In the FSCC sector (0,1), the Mg 3s and 3p orbitals were included in the model space. In MRCI, an analogous complete active space self-consistent field (CASSCF) reference was used with the complete active space usually designated as (1,4), i.e., one

TABLE X. Basis-set dependency of the transition (top) and permanent (below) dipole moments in ea_0 at the ground-state bond length and evaluated using the MRCI method.

Transition or state	v3z	ae3z	ae4z	s-aug.ae4z	d-aug.ae4z
$A\,^2\Pi_{1/2}$–$X\,^2\Sigma_{1/2}$	1.812	1.812	1.824	1.838	1.837
$A\,^2\Pi_{3/2}$–$X\,^2\Sigma_{1/2}$	1.812	1.812	1.824	1.838	1.837
$B\,^2\Sigma_{1/2}$–$X\,^2\Sigma_{1/2}$	1.527	1.527	1.530	1.517	1.499
$A\,^2\Pi_{3/2}$–$A\,^2\Pi_{1/2}$	0.001	0.001	0.001	0.001	0.001
$B\,^2\Sigma_{1/2}$–$A\,^2\Pi_{1/2}$	0.281	0.281	0.238	0.322	0.332
$B\,^2\Sigma_{1/2}$–$A\,^2\Pi_{3/2}$	0.281	0.281	0.238	0.322	0.332
$X\,^2\Sigma_{1/2}$	1.225	1.225	1.226	1.221	1.220
$A\,^2\Pi_{1/2}$	1.933	1.933	1.769	1.433	1.398
$A\,^2\Pi_{3/2}$	1.933	1.933	1.769	1.433	1.398
$B\,^2\Sigma_{1/2}$	1.309	1.309	0.787	0.005	0.265

TABLE XI. FCFs for the vibronic transitions between the upper (v') and lower (v'') electronic states.

	FCFs					
	$v'' = 0$	$v'' = 1$	$v'' = 2$	$v'' = 3$	$v'' = 4$	$v'' = 5$
$A^2\Pi_{1/2}$ — $X^2\Sigma_{1/2}$						
$v' = 0$	9.65×10^{-01}	3.37×10^{-02}	9.90×10^{-04}	3.07×10^{-05}	1.08×10^{-06}	4.59×10^{-08}
$v' = 1$	3.44×10^{-02}	8.97×10^{-01}	6.53×10^{-02}	2.94×10^{-03}	1.23×10^{-04}	5.48×10^{-06}
$v' = 2$	3.13×10^{-04}	6.81×10^{-02}	8.31×10^{-01}	9.47×10^{-02}	5.82×10^{-03}	3.08×10^{-04}
$v' = 3$	9.00×10^{-07}	9.66×10^{-04}	1.01×10^{-01}	7.66×10^{-01}	1.22×10^{-01}	9.55×10^{-03}
$v' = 4$	2.51×10^{-10}	3.80×10^{-06}	1.98×10^{-03}	1.33×10^{-01}	7.03×10^{-01}	1.46×10^{-01}
$v' = 5$	1.71×10^{-12}	1.11×10^{-09}	9.97×10^{-06}	3.36×10^{-03}	1.64×10^{-01}	6.44×10^{-01}
$A^2\Pi_{3/2}$ — $X^2\Sigma_{1/2}$						
$v' = 0$	9.65×10^{-01}	3.41×10^{-02}	1.01×10^{-03}	3.16×10^{-05}	1.12×10^{-06}	4.78×10^{-08}
$v' = 1$	3.48×10^{-02}	8.96×10^{-01}	6.61×10^{-02}	3.01×10^{-03}	1.27×10^{-04}	5.68×10^{-06}
$v' = 2$	3.23×10^{-04}	6.89×10^{-02}	8.29×10^{-01}	9.58×10^{-02}	5.94×10^{-03}	3.17×10^{-04}
$v' = 3$	9.54×10^{-07}	9.97×10^{-04}	1.02×10^{-01}	7.63×10^{-01}	1.23×10^{-01}	9.76×10^{-03}
$v' = 4$	2.98×10^{-10}	4.03×10^{-06}	2.04×10^{-03}	1.35×10^{-01}	7.00×10^{-01}	1.48×10^{-01}
$v' = 5$	1.76×10^{-12}	1.34×10^{-09}	1.06×10^{-05}	3.47×10^{-03}	1.65×10^{-01}	6.40×10^{-01}
$B^2\Sigma_{1/2}$ — $X^2\Sigma_{1/2}$						
$v' = 0$	8.66×10^{-01}	1.21×10^{-01}	1.19×10^{-02}	1.04×10^{-03}	8.63×10^{-05}	7.16×10^{-06}
$v' = 1$	1.27×10^{-01}	6.35×10^{-01}	2.02×10^{-01}	3.12×10^{-02}	3.71×10^{-03}	3.94×10^{-04}
$v' = 2$	6.19×10^{-03}	2.26×10^{-01}	4.53×10^{-01}	2.51×10^{-01}	5.42×10^{-02}	8.27×10^{-03}
$v' = 3$	1.11×10^{-04}	1.74×10^{-02}	3.00×10^{-01}	3.13×10^{-01}	2.75×10^{-01}	7.79×10^{-02}
$v' = 4$	4.93×10^{-07}	4.17×10^{-04}	3.24×10^{-02}	3.53×10^{-01}	2.08×10^{-01}	2.80×10^{-01}
$v' = 5$	2.04×10^{-11}	2.14×10^{-06}	9.68×10^{-04}	4.99×10^{-02}	3.88×10^{-01}	1.33×10^{-01}
$A^2\Pi_{3/2}$ — $A^2\Pi_{1/2}$						
$v' = 0$	$1.00 \times 10^{+00}$	1.72×10^{-06}	2.54×10^{-09}	1.58×10^{-11}	1.79×10^{-13}	5.13×10^{-15}
$v' = 1$	1.72×10^{-06}	$1.00 \times 10^{+00}$	3.50×10^{-06}	7.68×10^{-09}	6.48×10^{-11}	9.96×10^{-13}
$v' = 2$	2.30×10^{-09}	3.50×10^{-06}	$1.00 \times 10^{+00}$	5.34×10^{-06}	1.55×10^{-08}	1.67×10^{-10}
$v' = 3$	1.41×10^{-11}	6.95×10^{-09}	5.34×10^{-06}	$1.00 \times 10^{+00}$	7.25×10^{-06}	2.62×10^{-08}
$v' = 4$	1.58×10^{-13}	5.77×10^{-11}	1.40×10^{-08}	7.25×10^{-06}	$1.00 \times 10^{+00}$	9.18×10^{-06}
$v' = 5$	4.62×10^{-15}	8.80×10^{-13}	1.49×10^{-10}	2.37×10^{-08}	9.19×10^{-06}	$1.00 \times 10^{+00}$
$B^2\Sigma_{1/2}$ — $A^2\Pi_{1/2}$						
$v' = 0$	9.64×10^{-01}	3.48×10^{-02}	1.29×10^{-03}	4.83×10^{-05}	1.88×10^{-06}	7.76×10^{-08}
$v' = 1$	3.59×10^{-02}	8.95×10^{-01}	6.48×10^{-02}	3.64×10^{-03}	1.84×10^{-04}	9.03×10^{-06}
$v' = 2$	2.05×10^{-04}	6.92×10^{-02}	8.33×10^{-01}	9.04×10^{-02}	6.83×10^{-03}	4.34×10^{-04}
$v' = 3$	9.68×10^{-08}	5.66×10^{-04}	1.00×10^{-01}	7.76×10^{-01}	1.12×10^{-01}	1.06×10^{-02}
$v' = 4$	6.22×10^{-09}	5.62×10^{-07}	1.03×10^{-03}	1.28×10^{-01}	7.26×10^{-01}	1.29×10^{-01}
$v' = 5$	6.42×10^{-11}	3.06×10^{-08}	1.96×10^{-06}	1.52×10^{-03}	1.53×10^{-01}	6.84×10^{-01}
$B^2\Sigma_{1/2}$ — $A^2\Pi_{3/2}$						
$v' = 0$	9.64×10^{-01}	3.43×10^{-02}	1.26×10^{-03}	4.71×10^{-05}	1.81×10^{-06}	7.47×10^{-08}
$v' = 1$	3.54×10^{-02}	8.97×10^{-01}	6.40×10^{-02}	3.57×10^{-03}	1.79×10^{-04}	8.74×10^{-06}
$v' = 2$	1.97×10^{-04}	6.83×10^{-02}	8.35×10^{-01}	8.94×10^{-02}	6.70×10^{-03}	4.22×10^{-04}
$v' = 3$	1.08×10^{-07}	5.43×10^{-04}	9.88×10^{-02}	7.79×10^{-01}	1.10×10^{-01}	1.04×10^{-02}
$v' = 4$	5.99×10^{-09}	6.15×10^{-07}	9.84×10^{-04}	1.27×10^{-01}	7.30×10^{-01}	1.27×10^{-01}
$v' = 5$	6.57×10^{-11}	2.94×10^{-08}	2.10×10^{-06}	1.45×10^{-03}	1.51×10^{-01}	6.88×10^{-01}

electron in four MOs. In the MOLPRO MRCI calculation, we used a similar setup, except that all the virtual orbitals were correlated and the spin-orbit (SO) contribution was calculated *a posteriori* following a scalar relativistic MRCI calculation. The MRCI results obtained using the DIRAC and MOLPRO programs shown in Table IX agree very well so that there is no significant effect from the reduced virtual active space or the different treatment of the SO effects. For the PDMs, we

observe a good agreement between the two MRCI approaches as well as between MRCI and FSCC. The PDM of the excited $B^2\Sigma_{1/2}$ state is more sensitive to the basis-set size and the virtual cutoff compared to the lower states. However, this state is not the focus of the present study. Overall, the calculated values agree very well with the experimental ones.

The dipole moments (both permanent and transition) are found to be sensitive to the incompleteness of the basis set, as

shown in Table X. These were calculated at the equilibrium bond distance, using the MRCI approach in the MOLPRO program and freezing two electrons.

APPENDIX C: FRANCK-CONDON FACTORS

The FCFs were extracted from the calculated potential energy curves using the LEVEL16 [31] program. The potential was represented using 33 points on a nonequidistant grid (denser around the minimum) spanning the range between 1.5 Å to 2.2 Å. Cubic spline interpolation over $V(r)$ was used in the inner region and the extrapolation to the

dissociation limit was done by using four inverse power terms (r^0 to r^3). During our previous study on the heavier homologues CaF, SrF, and BaF [32], we investigated the errors introduced in the numerical scheme in more detail. This setup turned out to be robust and the final results are rather insensitive to the choice of interpolation and extrapolation scheme.

Table XI presents the FCFs for the vibronic transitions between the ground and excited electronic states of the MgF molecule. We used the potential energy surfaces obtained at the 4c-FSCC(0,1) level of theory and the d-aug-dyall.ae4z basis set (with CP and ΔT corrections), and extracted the FCFs from the LEVEL16 [31] program.

[1] L. Anderegg, B. L. Augenbraun, Y. Bao, S. Burchesky, L. W. Cheuk, W. Ketterle, and J. M. Doyle, Laser cooling of optically trapped molecules, Nat. Phys. **14**, 890 (2018).

[2] S. Ding, Y. Wu, I. A. Finneran, J. J. Burau, and J. Ye, Sub-Doppler Cooling and Compressed Trapping of YO Molecules at μK Temperatures, Phys. Rev. X **10**, 021049 (2020).

[3] M. Tomza, Energetics and Control of Ultracold Isotope-Exchange Reactions between Heteronuclear Dimers in External Fields, Phys. Rev. Lett. **115**, 063201 (2015).

[4] Y. Liu, D. D. Grimes, M.-G. Hu, and K.-K. Ni, Probing ultracold chemistry using ion spectrometry, Phys. Chem. Chem. Phys. **22**, 4861 (2020).

[5] S. Jurgilas, A. Chakraborty, C. J. H. Rich, L. Caldwell, H. J. Williams, N. J. Fitch, B. E. Sauer, M. D. Frye, J. M. Hutson, and M. R. Tarbutt, Collisions between Ultracold Molecules and Atoms in a Magnetic Trap, Phys. Rev. Lett. **126**, 153401 (2021).

[6] S. V. Alyabyshev, M. Lemeshko, and R. V. Krems, Sensitive imaging of electromagnetic fields with paramagnetic polar molecules, Phys. Rev. A **86**, 013409 (2012).

[7] E. B. Norrgard, S. P. Eckel, C. L. Holloway, and E. L. Shirley, Quantum blackbody thermometry, New J. Phys. **23**, 033037 (2021).

[8] D. DeMille, Quantum Computation with Trapped Polar Molecules, Phys. Rev. Lett. **88**, 067901 (2002).

[9] S. Moses, J. Covey, M. Miecnikowski, D. Jin, and J. Ye, New frontiers for quantum gases of polar molecules, Nat. Phys. **13**, 13 (2017).

[10] J. A. Blackmore, L. Caldwell, P. D. Gregory, E. M. Bridge, R. Sawant, J. Aldegunde, J. Mur-Petit, D. Jaksch, J. M. Hutson, B. E. Sauer, M. R. Tarbutt, and S. L. Cornish, Ultracold molecules for quantum simulation: Rotational coherences in CaF and RbCs, Quantum Sci. Technol. **4**, 014010 (2018).

[11] H. Son, J. J. Park, W. Ketterle, and A. O. Jamison, Collisional cooling of ultracold molecules, Nature (London) **580**, 197 (2020).

[12] J. F. Barry, E. S. Shuman, E. B. Norrgard, and D. DeMille, Laser Radiation Pressure Slowing of a Molecular Beam, Phys. Rev. Lett. **108**, 103002 (2012).

[13] D. DeMille, J. F. Barry, E. R. Edwards, E. B. Norrgard, and M. H. Steinecker, On the transverse confinement of radiatively slowed molecular beams, Mol. Phys. **111**, 1805 (2013).

[14] M. Di Rosa, Laser-cooling molecules, Eur. Phys. J. D **31**, 395 (2004).

[15] W. Jevons, Observations in connection with the band systems of the fluorides of beryllium and magnesium, Proc. R. Soc. London, Ser. A **122**, 211 (1929).

[16] F. A. Jenkins and R. Grinfeld, The spectrum of MgF, Phys. Rev. **45**, 229 (1934).

[17] M. Pelegrini, C. S. Vivacqua, O. Roberto-Neto, F. R. Ornellas, and F. B. C. Machado, Radiative transition probabilities and lifetimes for the band systems $A\,^2\Pi - X\,^2\Sigma^+$ of the isovalent molecules BeF, MgF and CaF, Braz. J. Phys. **35**, 950 (2005).

[18] L. Xu, Y. Yin, B. Wei, Y. Xia, and J. Yin, Calculation of vibrational branching ratios and hyperfine structure of ^{24}Mg ^{19}F and its suitability for laser cooling and magneto-optical trapping, Phys. Rev. A **93**, 013408 (2016).

[19] I. Singh, M. Shukla, and R. Maheshwari, Vibrational transition probabilities and r-centroids for the A-X system of the magnesium fluoride molecule, J. Quant. Spectrosc. Radiat. Transfer **9**, 533 (1969).

[20] S. Kang, Y. Gao, F. Kuang, T. Gao, J. Du, and G. Jiang, Theoretical study of laser cooling of magnesium monofluoride using ab initio methods, Phys. Rev. A **91**, 042511 (2015).

[21] C. Zhang, B. Augenbraun, Z. D. Lasner, N. B. Vilas, J. M. Doyle, and L. Cheng, Accurate prediction and measurement of vibronic branching ratios for laser cooling linear polyatomic molecules, J. Chem. Phys. **155**, 091101 (2021).

[22] M. Doppelbauer, S. C. Wright, S. Hofsäss, B. G. Sartakov, G. Meijer, and S. Truppe, Hyperfine-resolved optical spectroscopy of the $A^2\Pi \leftarrow X^2\Sigma^+$ transition in MgF, J. Chem. Phys. **156**, 134301 (2022).

[23] B. K. Stuhl, B. C. Sawyer, D. Wang, and J. Ye, Magneto-optical Trap for Polar Molecules, Phys. Rev. Lett. **101**, 243002 (2008).

[24] K. G. Dyall, Relativistic double-zeta, triple-zeta, and quadruple-zeta basis sets for the light elements H–Ar, Theor. Chem. Acc. **135**, 128 (2016).

[25] T. Saue, R. Bast, A. S. P. Gomes, H. J. A. Jensen, L. Visscher, I. A. Aucar, R. Di Remigio, K. G. Dyall, E. Eliav, E. Fasshauer *et al.*, The DIRAC code for relativistic molecular calculations, J. Chem. Phys. **152**, 204104 (2020).

[26] R. Bast, A. S. P. Gomes, T. Saue, L. Visscher, and H. J. Aa. Jensen, with contributions from I. A. Aucar, V. Bakken, C. Chibueze, J. Creutzberg, K. G. Dyall, S. Dubillard, U. Ekström, E. Eliav, T. Enevoldsen, E. Faßhauer *et al.*, DIRAC, a relativistic *ab initio* electronic structure program, Release DIRAC23, Zenodo (2023), doi: https://doi.org/10.5281/zenodo.7670749, see also https://www.diracprogram.org.

[27] J. Dunham, The energy levels of a rotating vibrator, Phys. Rev. **41**, 721 (1932).

[28] G. Herzberg, *Molecular Spectra and Molecular Structure-Vol I*, (Read Books, Nedlands, Australia, 2013).

[29] R. W. Nicholls and W. R. Jarmain, r-centroids: Average internuclear separations associated with molecular bands, Proc. Phys. Soc. London, Sect. A **69**, 253 (1956).

[30] H.-J. Werner, P. J. Knowles, G. Knizia, F. R. Manby, M. Schütz *et al.*, MOLPRO, version 2022.02, a package of *ab initio* programs.

[31] R. J. Le Roy, LEVEL: A computer program for solving the radial Schrödinger equation for bound and quasibound levels, J. Quant. Spectrosc. Radiat. Transfer **186**, 167 (2017).

[32] Y. Hao, L. F. Pašteka, L. Visscher, P. Aggarwal, H. L. Bethlem, A. Boeschoten, A. Borschevsky, M. Denis, K. Esajas, S. Hoekstra *et al.*, High accuracy theoretical investigations of CaF, SrF, and BaF and implications for laser-cooling, J. Chem. Phys. **151**, 034302 (2019).

[33] B. Barber, K. Zhang, B. Guo, and P. Bernath, Vibration-rotation emission spectrum of MgF, J. Mol. Spectrosc. **169**, 583 (1995).

[34] R. F. Barrow and J. R. Beale, Rotational analysis of electronic bands of gaseous MgF, Proc. Phys. Soc. **91**, 483 (1967).

[35] J. Gu, Z. Xiao, C. Yu, Q. Zhang, Y. Chen, and D. Zhao, High resolution laser excitation spectra and franck-condon factors of $A\,^2\Pi$- $X\,^2\Sigma^+$ electronic transition of MgF, Chin. J. Chem. Phys. **35**, 58 (2022).

[36] E. B. Norrgard, D. S. Barker, S. P. Eckel, S. G. Porsev, C. Cheung, M. G. Kozlov, I. I. Tupitsyn, and M. S. Safronova, Laser spectroscopy of the $y\,^7P_J^o$ states of Cr I, Phys. Rev. A **105**, 032812 (2022).

[37] M. Wahl, T. Röhlicke, S. Kulisch, S. Rohilla, B. Krämer, and A. C. Hocke, Photon arrival time tagging with many channels, sub-nanosecond deadtime, very high throughput, and fiber optic remote synchronization, Rev. Sci. Instrum. **91**, 013108 (2020).

[38] P. T. Starkey, C. J. Billington, S. P. Johnstone, M. Jasperse, K. Helmerson, L. D. Turner, and R. P. Anderson, A scripted control system for autonomous hardware-timed experiments, Rev. Sci. Instrum. **84**, 085111 (2013).

[39] J. F. Barry, E. S. Shuman, and D. DeMille, A bright, slow cryogenic molecular beam source for free radicals, Phys. Chem. Chem. Phys. **13**, 18936 (2011).

[40] S. Truppe, M. Hambach, S. M. Skoff, N. E. Bulleid, J. S. Bumby, R. J. Hendricks, E. A. Hinds, B. E. Sauer, and M. R. Tarbutt, A buffer gas beam source for short, intense and slow molecular pulses, J. Mod. Opt. **65**, 648 (2018).

[41] L. R. Hunter, S. K. Peck, A. S. Greenspon, S. S. Alam, and D. DeMille, Prospects for laser cooling TlF, Phys. Rev. A **85**, 012511 (2012).

[42] E. B. Norrgard, E. R. Edwards, D. J. McCarron, M. H. Steinecker, D. DeMille, S. S. Alam, S. K. Peck, N. S. Wadia, and L. R. Hunter, Hyperfine structure of the $B\,^3\Pi_1$ state and predictions of optical cycling behavior in the $X \rightarrow B$ transition of TlF, Phys. Rev. A **95**, 062506 (2017).

[43] J. M. Houston, C. J. Zarobila, and H. W. Yoon, Achievement of 0.005% combined transfer uncertainties in the nist detector calibration facility, Metrologia **59**, 025001 (2022).

[44] D. Allen, E. Early, B. Tsai, and C. Cooksey, *NIST Measurement Services: Regular Spectral Transmittance*, NIST Special Publication 250-69 (U.S. Department of Commerce, Washington, DC, 2011).

[45] Any mention of commercial products within this work is for information only; it does not imply recommendation or endorsement by NIST.

[46] M. Patting, M. Wahl, P. Kapusta, and R. Erdmann, Dead-time effects in TCSPC data analysis, in *Photon Counting Applications, Quantum Optics, and Quantum Cryptography*, Vol. 6583, edited by M. Dusek, M. S. Hillery, W. P. Schleich, I. Prochazka, A. L. Migdall, and A. Pauchard, International Society for Optics and Photonics (SPIE, Washington, D.C., 2007), pp. 72–81.

[47] B. Klöter, C. Weber, D. Haubrich, D. Meschede, and H. Metcalf, Laser cooling of an indium atomic beam enabled by magnetic fields, Phys. Rev. A **77**, 033402 (2008).

[48] E. B. Norrgard, D. J. McCarron, M. H. Steinecker, M. R. Tarbutt, and D. DeMille, Submillikelvin Dipolar Molecules in a Radio-Frequency Magneto-Optical Trap, Phys. Rev. Lett. **116**, 063004 (2016).

[49] E. B. Norrgard, Magneto-optical trapping of diatomic molecules, Ph.D. thesis, Yale University, 2016.

[50] S. Eckel, D. S. Barker, E. B. Norrgard, and J. Scherschligt, PYLCP: A python package for computing laser cooling physics, Comput. Phys. Commun. **270**, 108166 (2022).

[51] B. Hemmerling, G. K. Drayna, E. Chae, A. Ravi, and J. M. Doyle, Buffer gas loaded magneto-optical traps for Yb, Tm, Er and Ho, New J. Phys. **16**, 063070 (2014).

[52] J. C. Shaw and D. J. McCarron, Bright, continuous beams of cold free radicals, Phys. Rev. A **102**, 041302(R) (2020).

[53] K. J. Rodriguez, N. H. Pilgram, D. S. Barker, S. P. Eckel, and E. B. Norrgard, companion paper, Simulations of a frequency-chirped magneto-optical trap of MgF, Phys. Rev. A **108**, 033105 (2023).

[54] A. V. Oleynichenko, A. Zaitsevskii, and E. Eliav, Towards high performance relativistic electronic structure modelling: The exp-t program package, *Supercomputing: 6th Russian Supercomputing Days, RuSCDays 2020, Moscow, Russia, September 21–22, 2020, Revised Selected Papers 6* (Springer, New York, 2020), pp. 375–386.

[55] A. V. Oleynichenko, A. Zaitsevskii, and E. Eliav, EXP-T, An Extensible Code for Fock Space Relativistic Coupled Cluster Calculations.

[56] S. F. Boys and F. Bernardi, The calculation of small molecular interactions by the differences of separate total energies. some procedures with reduced errors, Mol. Phys. **19**, 553 (1970).

[57] A. Sunaga, M. Salman, and T. Saue, 4-component relativistic Hamiltonian with effective QED potentials for molecular calculations, J. Chem. Phys. **157**, 164101 (2022).

[58] A. S. P. Gomes, T. Saue, L. Visscher, H. J. Aa. Jensen, and R. Bast, with contributions from I. A. Aucar, V. Bakken, K. G. Dyall, S. Dubillard, U. Ekström, E. Eliav, T. Enevoldsen, E. Faßhauer, T. Fleig, O. Fossgaard *et al.*, DIRAC, a relativistic *ab initio* electronic structure program, Release DIRAC19, Zenodo (2019), doi: https://doi.org/10.5281/zenodo.7670749, see also https://www.diracprogram.org..